Chapter 3
Electronic Structure and Magnetism of Correlated Nanosystems

Alexander Lichtenstein, Maria Valentyuk, Roberto Mozara and Michael Karolak

Abstract Magnetic nanostructures based on transition metals represent a main building block of standard memory devices. Their unique electronic properties are related to a complex multiplet structure of the partially filled d-shell with strong Coulomb interactions. Starting from a general formulation of the effective multi-orbital impurity problem for a transition metal atom in a fermionic bath of conduction electrons, the exact Quantum Monte Carlo solution is discussed. The concept of Hund's impurities to describe the electronic structure and magnetism of transition metal adatoms becomes very useful for the interpretation of numerous experimental data.

3.1 Electron Correlations in Magnetic Nanosystems

Transition metal atoms and small clusters on metallic substrates represent unique quantum systems to study complex many-body physics beyond standard mean-field electronic theories [1]. Recent progress in solid state theory allows for the analysis of the electronic structure and magnetic properties of correlated systems, while taking into account realistic dynamical many-body effects. These new approaches unify the Stoner theory of itinerant electron magnetism with the Heisenberg model for local spin systems into a unique spin-fluctuation Hubbard approach for real multi-orbital complex materials (see Fig. 3.1). Using the calculated electronic structure of different materials enables one to analyse magnetic properties and effective exchange interactions [2]. Understanding the properties of transition metal ions in different environments is a key ingredient and starting point for the modern theory of magnetism. The tremendous progress over the last years in experimental fabrication of new classes of materials, such as iron-based superconductors, magnetoresistance

A. Lichtenstein (✉) · M. Valentyuk · R. Mozara · M. Karolak
I. Institute of Theoretical Physics, Hamburg University, Hamburg, Germany
e-mail: alichten@physnet.uni-hamburg.de

© Springer Nature Switzerland AG 2018

R. Wiesendanger (ed.), *Atomic- and Nanoscale Magnetism*, NanoScience and Technology, https://doi.org/10.1007/978-3-319-99558-8_3

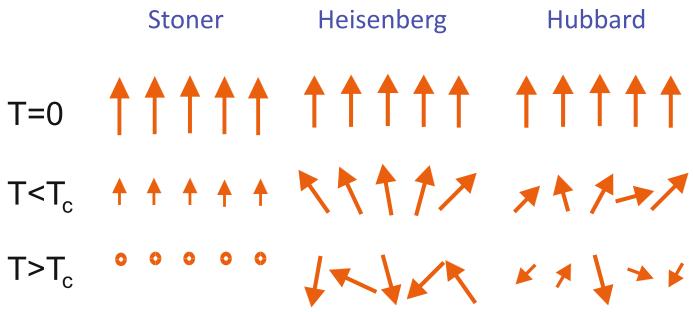

Fig. 3.1 Outline of classical magnetic models for different temperatures: Stoner theory of weakly correlated itinerant electrons, Heisenberg theory of local spin systems and Hubbard theory of spin and charge fluctuations in transition metal systems

systems, and two-dimensional artificial super-lattices put forward new challenges to the theory of transition metal systems. It is well known that the ground-state properties of antiferromagnetic insulators or compounds with orbital ordering cannot be obtained within the standard density functional theory (DFT) [2]. Recent angle-resolved photoemission studies of different cuprate materials [3] pointed out the existence of so-called incoherent peaks in the spectral density, which signals the strong inter-electron correlations in transition metal compounds.

The origin of such complicated features in the spectral properties of correlated materials is connected with the strong excitations to various low-energy electronic configurations, which are represented as a general pattern in Fig. 3.2. Let us discuss one common situation in which the free energy of correlated materials has one well-separated non-magnetic ground state. In this case, it is clear that electron fluctuations will be very small at low temperatures which results in the standard nonmagnetic quasiparticle structure. In opposing situations, when there are few closed local minima corresponding to different spin and orbital structures, as depicted in Fig. 3.2, we can be sure that strong many-body fluctuations will result in a non-quasiparticle structure of the spectral density, originating from Hund's rule behavior [4]. In order to describe systems with such a complicated energy spectrum, one has to use general quantum path-integral methods [5] and investigate different correlation functions using the recently developed continuous-time quantum Monte Carlo schemes [6], which efficiently describe different local minima of the free-energy functional (Fig. 3.2).

The complicated example of ferromagnetic iron with long-range exchange interactions [8] shows important quantum magnetic fluctuations at high temperature and high pressure [7]. So-called half-metallic ferromagnets [9] can be a playground for interesting magnetic correlation effects related to non-quasiparticle states in the minority-spin gap [10] which in principle can be detected in tunneling experiments [11]. Ultrafast dynamics of spin systems [12] and spin-spin correlations in magnetic systems [13] represent future directions of research.

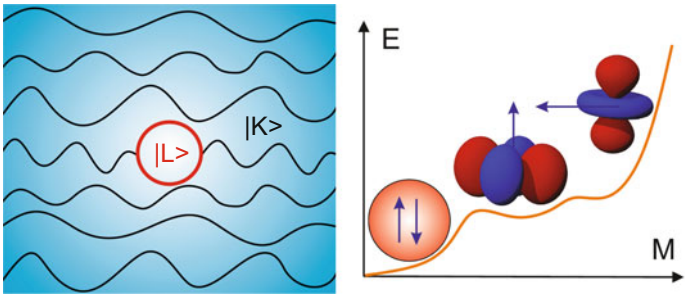

Fig. 3.2 Left: Simple view of the projection technique from itinerant Bloch states $|K\rangle$ to a localised Wannier basis $|L\rangle$ of a correlated subset. Right: Scheme of multiple local minima for nonmagnetic, magnetic and orbital states for strongly interacting electron materials

3.2 Realistic Impurity Models for Correlated Electron Systems

We developed a general scheme for partitioning the local orbital degrees of freedom, which provides practical tools for the investigation of different magnetic adatoms on metallic substrates. In the case of classical Kondo systems, based on cobalt adatoms on the gold surface, these local orbitals are related to the $3d$ electrons of the Co atom. Only a few electronic states from the total basis are needed to be taken into account in the many-body treatment. One of the most useful electronic structure approaches was thus related to the projector scheme which separates the total basis into the subset of Bloch states describing the standard itinerant electrons $|K\rangle$, and these local correlated d orbitals $|L\rangle$ represented by a numerical Wannier basis (see Fig. 3.2 for simple illustration).

In order to use the Monte-Carlo method for correlated subsystems one first needs to calculate the local Green functions and hybridization functions for the five local d orbitals. Standard density functional computer codes use a plane-wave basis set $|K\rangle$. In this case the transformation of the basis set is straightforward, and the convergence properties are easy to control. One of the most precise and efficient plane-wave based approaches is related to the projector augmented wave (PAW) method [14] and was successfully used in the general projection scheme from the Bloch itinerant basis to the local orbital states, seen in Fig. 3.2, using the overlap matrix $\langle K|L\rangle$.

Our universal projection scheme is based on the implementation of a projection operator $\mathcal{P} = \sum_L |L\rangle \langle L|$ within a DFT+DMFT method which is described in detail in [15–17]. Using this projector it is easy to transform the full Kohn–Sham Green function $G^K(\omega)$ into a set of five d orbitals $\{|L\rangle\}$:

$$G^L(\omega) = \mathcal{P} G^K(\omega). \tag{3.1}$$

The subspace $\{|L\rangle\}$ will represent the local correlated d-orbitals. Only these five d orbitals will be used in the many-body investigations which produce the important

corrections to the DFT spectrum due to electronic fluctuations. Within the plane-wave scheme, the Bloch Green's function $G^K(\omega)$ with the Matsubara frequencies $i\omega$ can be calculated in terms of the complete basis of Bloch states $|K\rangle$. The Bloch states represent the solution of the general Kohn–Sham eigenvalue problem for an effective Hamiltonian H_K, with

$$H_K\,|K\rangle = \varepsilon_K\,|K\rangle\,. \tag{3.2}$$

Using (3.1) and (3.2), and the definition of projections overlap $\langle L|K\rangle$, one can easily evaluate the Green's function in the local basis $|L\rangle$ with a given chemical potential μ as

$$G^L(i\omega) = \sum_K \frac{\langle L|K\rangle\langle K|L\rangle}{i\omega + \mu - \varepsilon_K}. \tag{3.3}$$

For magnetic transition metal adatoms on different surfaces the set of correlated states are represented by five d orbitals. These correlated orbitals are located mostly inside PAW augmentation spheres (Fig. 3.2) which allowed us to use the standard representation of a Bloch state $|K\rangle$ projection onto local five d orbitals [14]. If we use only a small number of bands near the Fermi energy for projection onto the local impurity orbitals, it is important to properly orthogonalize the local basis functions [15, 16].

We can define the effective hybridization matrix $\Delta(i\omega)$ for the d orbitals impurity model using the following equation for the local Green's function

$$G^{-1}(i\omega) = i\omega - \epsilon_d - \Delta(i\omega). \tag{3.4}$$

The impurity energy ϵ_d describes the crystal field effects from substrates. In general, (3.4) represents a $L \times L$ matrix equation for Δ. In order to separate the static DFT crystal field energy ϵ_d from the frequency dependent hybridization function Δ, one normally evaluates the limit $\omega \to \infty$, where $\Delta(i\omega) \to 0$, and therefore $G^{-1}(i\omega) \to i\omega - \epsilon_d$.

3.3 Multiorbital Quantum Impurity Solvers

The formulation of a numerical solution to the multi-orbital impurity model was a challenge for the quantum many-body problems. During the last decade we developed the novel continuous-time quantum Monte-Carlo (CT-QMC) solver [6] for the general multi-orbital impurity problem. The CT-QMC scheme is based on stochastic Monte-Carlo sampling and consists of two complementary approaches: the interaction and the hybridization expansion. We describe here the most efficient approach for the strongly correlated case, which is the hybridization algorithm (CT-HYB). For simplicity, we discuss the so-called segment scheme, which allows for a fast

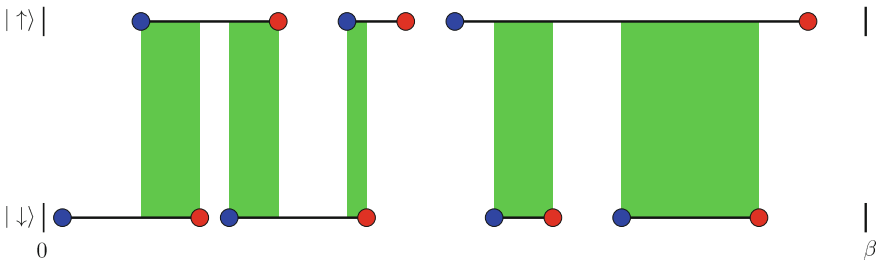

Fig. 3.3 Example of a single-orbital CT-HYB expansion in the segment formalism: The annihilation operators are represented by the blue dots and the creation operators by red ones. The black lines describe hybridization functions $\Delta(\tau_i - \tau'_j)$ for two spin projections. The time interval in which two electrons are present on the impurity is marked by a green region with total time l_d, and consequently an energy penalty of U has to be payed here

analytical evaluation of the path-integral trace for d-electrons in the case of diagonal-density types of Coulomb interaction.

The quantum impurity problem at temperature β^{-1} can be represented by the action

$$S_{\text{imp}} = S_{\text{at}} + S_{\Delta} \tag{3.5}$$

with the atomic component

$$S_{\text{at}} = \sum_{\sigma} \int_0^{\beta} \mathrm{d}\tau c^*_{\sigma\tau}[\partial_\tau - \mu]c_{\sigma\tau} + \int_0^{\beta} \mathrm{d}\tau U n_{\uparrow\tau} n_{\downarrow\tau} \tag{3.6}$$

where $c^*_{\sigma\tau}$, $c_{\sigma\tau}$ are Grassmann variables which depend on spin σ, and τ is the imaginary time space. For simplicity we skip orbital indices and $n_{\sigma\tau} = c^*_{\sigma\tau} c_{\sigma\tau}$. The hybridization action S_{Δ} contains the term $\Delta(\tau)$, and can be written as

$$S_{\Delta} = \sum_{\sigma} \int_0^{\beta} \int_0^{\beta} \mathrm{d}\tau \mathrm{d}\tau' c^*_{\sigma\tau} \Delta(\tau - \tau') c_{\sigma\tau'} \,, \tag{3.7}$$

and is the Fourier transform of the $\Delta(i\omega)$ matrix.

To simplify the notation, we suppress the spin indices and view the proceeding expressions as diagonal matrices in spin and orbital space. We expand the impurity action (3.5) in the hybridization part (3.7) around the atomic limit (3.6). It can then be found, that at a given perturbation order k of the hybridization expansion of the impurity action S_{imp} in power of S_{Δ}, different terms can be combined into a determinant of hybridization functions. Therefore, the impurity partition function may be written in the following form:

$$\mathcal{Z}/\mathcal{Z}_{\text{at}} = \sum_k \int_0^{\beta} \mathrm{d}\tau_1 \ldots \int_{\tau_{k-1}}^{\beta} \mathrm{d}\tau_k \langle c^*_{\tau_1} \ldots c_{\tau_k} \rangle_{\text{at}} \det \hat{\Delta}^{(k)}. \tag{3.8}$$

The average trace $\langle c^*_{\tau_1} \dots c_{\tau_k} \rangle_{\rm at}$ in this expression should be calculated over exact states of the atomic action $S_{\rm at}$. In principle, this can be done numerically for an arbitrarily complicated multi-orbital interaction matrix U [6].

The hybridization matrix determinant $\det \hat{\Delta}^{(k)}$ consists of a $k \times k$ matrix in imaginary time space $\hat{\Delta}_{ij} = \Delta(\tau_i - \tau_j)$. Assembling the $k!$ different terms into a single hybridization determinant is crucial for the suppression of the so-called fermionic sign problem in CT-QMC [6]. One should point out that the time interval in imaginary space of equation (3.8) can be considered as a circle with antiperiodic (fermionic) boundary conditions.

In the simplest case of a single-orbital impurity model with Hubbard interaction (3.6), the segment formalism gives a very intuitive picture of CT-QMC insertion in imaginary τ-space in the interval $[0, \beta]$, which is shown in Fig. 3.3. An arbitrary configuration can be represented by two separate world-lines for different spins. In this scheme one can exactly calculate the impurity trace which is related to contributions from the chemical potential μ and the Hubbard-U interaction term for time-intervals of double occupancy on the impurity, and resulting in the simple expression $e^{-U l_d + \mu(l_\uparrow + l_\downarrow)}$, where l_σ represents the time spent by a spin-σ electron on the impurity, and l_d corresponds to the total time of a doubly occupied impurity state [6].

3.4 Transition Metal Impurities on Metallic Substrates

Using the continuous-time quantum Monte Carlo methods within the interaction (CT-INT) [18] or hybridization (CT-HYB) expansion [19], we investigated accurate low-temperature spectral functions of transition metal impurities on metallic substrates. As an example, we present the electronic structure of cobalt atoms on the Cu(111) surface based on realistic DFT supercell calculations, in combination with the many-body CT-QMC investigation of the multi-orbital local impurity problem [19].

The electronic structure of the cobalt adatom on the Cu(111) surface was first analyzed within a large supercell scheme of twelve atoms in a plane with a thickness of five atomic layers, using the PAW scheme [14] (see Fig. 3.4). Using (3.4) and results of DFT calculations we obtained the hybridization functions shown in Fig. 3.4 for orbitals within the local C_{3v} point group symmetry. The five Co d orbitals split into three subblocks of two doubly degenerate and one non-degenerate representations with corresponding orbitals d_{xz}, d_{yz} for the E_1 representation, $d_{x^2-y^2}$, d_{xy} for E_2, and d_{z^2} for A_1, respectively. A full four-index Coulomb correlation vertex U for the five d orbitals [2] was obtained via screened Slater parameters F^0, F^2, and F^4 corresponding to an effective Hubbard parameter $U = 4\,\text{eV}$ and to a Hund interaction $J = 0.9\,\text{eV}$.

Since the hybridization of a cobalt atom with the substrate Cu(111) is rather weak (Fig. 3.4), the correlation effects will be strong. The results of the many-body CT-QMC calculations for the density of states (DOS) shows the corresponding new features. There is strong renormalization of the DFT quasiparticle structure near $E_{\rm F}$,

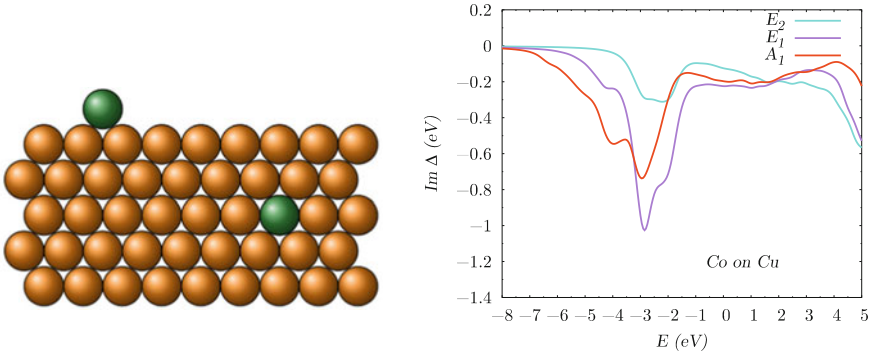

Fig. 3.4 Left: Sketch of cobalt impurities on top of a copper surface and in the bulk. Right: the imaginary parts of the hybridization functions Im Δ for different orbital symmetries

producing sharp Kondo-like peaks, and at higher energies the formation of lower and upper Hubbard bands is clearly visible (Fig. 3.5). One can also see the strong anisotropy of the local DOS of Co on Cu(111) for the different orbitals belonging to the E_1, E_2, and A_1 representations. The smallest hybridization function corresponds to orbitals of E_2 symmetry located in the x-y plane and therefore atomic-like Hubbard bands are well pronounced with the strong suppression of the quasiparticle peak at E_F. We noted that the low-energy quasi-particle peaks appear in all five Co d orbitals, which was not expected within the model for the two-channel Kondo problem for spin $S = 1$, which was assumed to apply for the Co adatom, and where the resonance at E_F would appear within two orbitals only.

The formation of a local Fermi-liquid state of Co on Cu for all five d orbitals at low-temperature indicate a strong hybridization with the metallic substrate. For the estimation of the Kondo temperature T_K one can use the quasiparticle renormalization factor Z calculated from the CT-QMC scheme and a general result from the single impurity Anderson model [20]: $T_K = -\frac{\pi}{4} Z \,\mathrm{Im}\,\Delta(0)$. The corresponding Kondo temperatures within the irreducible representations are: $T_K = 60\,\mathrm{K}$ in E_2, $T_K = 310\,\mathrm{K}$ in E_1, and $T_K = 180\,\mathrm{K}$ in A_1, and the agreement with the experimental result $T_K \approx (54 \pm 5)\,\mathrm{K}$ is reasonable [21]. We were also able to reproduce the large difference of the Kondo scale for the impurity in the bulk and the adatom on the surface [19]. To our knowledge, this is the first successful calculation of the Kondo temperature for a realistic correlated impurity with five orbitals.

3.5 Hund's Impurities on Substrates

The magnetic behavior and electronic structure of d-metal impurities in the fermionic bath of the substrate crucially depends on the multiplet structures and Hund's rule physics [4]. In order to show such Hund's effects we investigated single Mn, Fe,

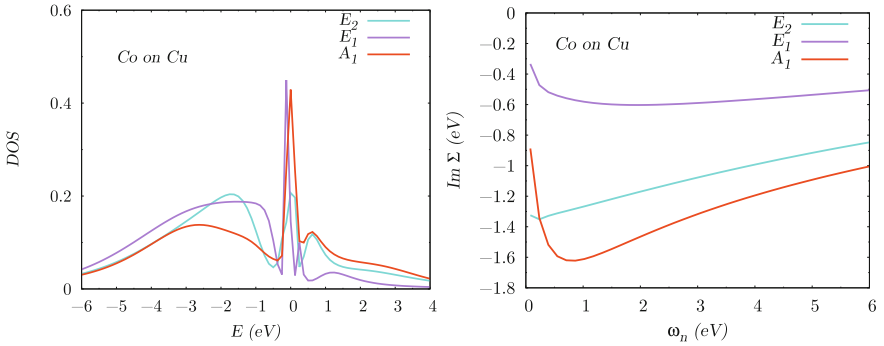

Fig. 3.5 Left: Orbitally resolved DOS of the Co impurities on Cu obtained by analytical continuation of the CT-QMC imaginary time Green's function for $\beta = 40$ eV^{-1}. Right: **a** corresponding orbitally resolved self-energies on the Matsubara axis

Co and Ni adatoms on the metallic Ag(100) surface [22]. The experimental photoemission spectra for the $3d$ series shows a monotonous reduction of high-energy splittings together with non-monotonous features at low-energy peaks. We can now explain this behavior by means of Hund's physics. On the one hand, the high-energy peaks are related to splitting of the ground state energy into multiplets with different spin quantum numbers, to a monotonous decrease of the local magnetic moment m, and to the Hund's splittings Jm which monotonously decrease to the end of the $3d$ series due to filling of the d band. On the other hand, the effective Hubbard energies $U = E_{n+1} + E_{n-1} - 2E_n$ [2, 4], (where E_n is the impurity ground state energy with n particles) has strongly non-monotonous variation in the $3d$ series related to Hund's rules physics.

Using a rotationally invariant Coulomb interaction matrix [2] one can find a strong dependence of the effective Hubbard parameter $\tilde{U}$ as a function of $3d$-occupation n:

$$\tilde{U} \approx \begin{cases} U + 4J & (n = 5) \\ U - 3J/2 & (n = 6, 9) \\ U - J/2 & (n = 7, 8). \end{cases} \tag{3.9}$$

From these results we were able to make a conclusion about the non-monotonous behavior of the charge fluctuations and the renormalization of the DOS at E_F which depends on the effective Hubbard parameter $\tilde{U}$ in the $3d$ series. Our results show strong charge fluctuations for Fe ($n = 6$) and Ni ($n = 9$) related to the almost mixed-valence regime due to the small value of $\tilde{U}$. For the case of Mn ($n = 5$) and Co ($n = 7$) the Hubbard parameter U is much larger, which suppresses the charge fluctuations and promotes the multi-orbital Kondo behavior.

Figure 3.6 shows the valence photoemission spectrum for Mn, Fe, Co and Ni adatoms on the silver surface together with theoretical QMC results of the corresponding impurity problem containing first-principle hybridization functions [22]. The Mn ($n = 5$) impurity has the largest effective interaction U (3.9), and the single

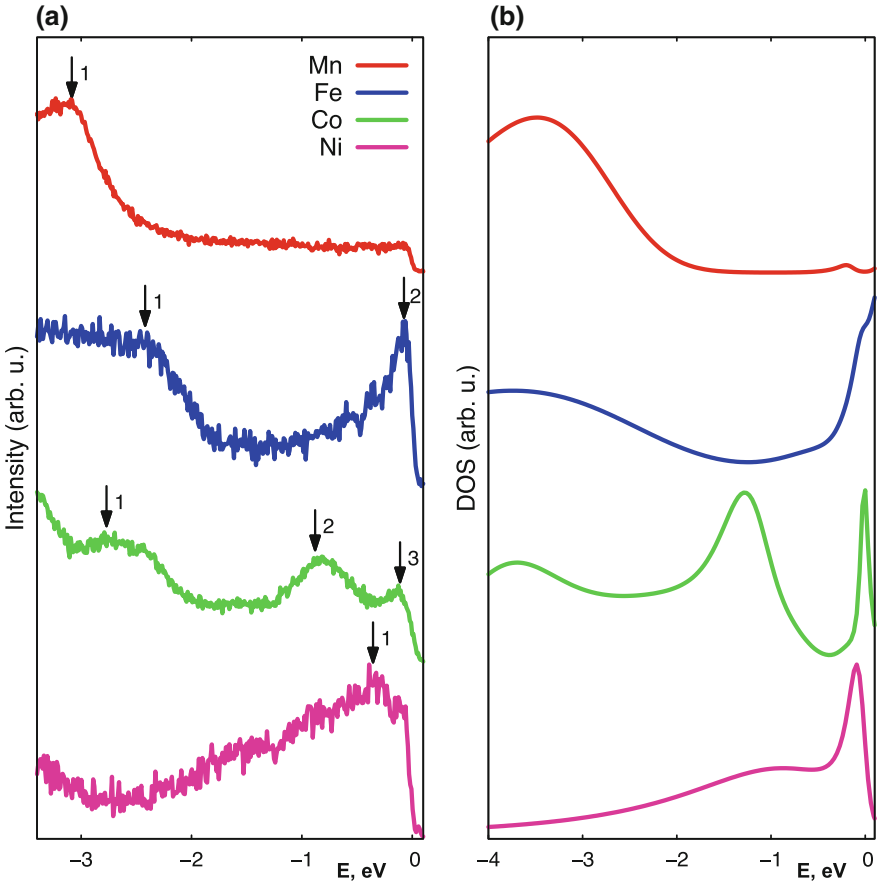

Fig. 3.6 **a** Experimental valence electron photoemission spectra of $3d$ adatoms on Ag(100) surface. **b** Theoretical spectral function from QMC results at $\beta = 20\,\mathrm{eV}^{-1}$

multiplet spectrum for the maximum-spin ground state $S = 5/2$ can explain the single high-energy peak at -3.5 eV in the spectral function. For the Fe ($n = 6$) impurity, the calculations show a broad lower-Hubbard band at -3 eV and a sharp quasiparticle resonance below E_F, and can be well compared with the experimental peaks 1 and 2 (Fig. 3.6a). This broad Hubbard band at -3 eV is formed by all $3d$ orbitals and can be found in simple atomic exact diagonalization (ED) results, and is related to $d^6 \rightarrow d^5$ excitations (Fig. 3.6b). From the orbitally resolved DOS in Fig. 3.6b one can identify the $d_{x^2-y^2}$ orbital which is responsible for the experimental peak 2 (Fig. 3.6a). The occupation of the $d_{x^2-y^2}$ orbital is equal to $n = 0.8$ due to strong charge fluctuations in the Fe $3d$ shell and indicates that this peak is not related to a spin-Kondo resonance. If one inspects the atomic ED calculations for the Fe impurity with crystal field splitting from the surface hybridization (Fig. 3.6b), this peak also results from

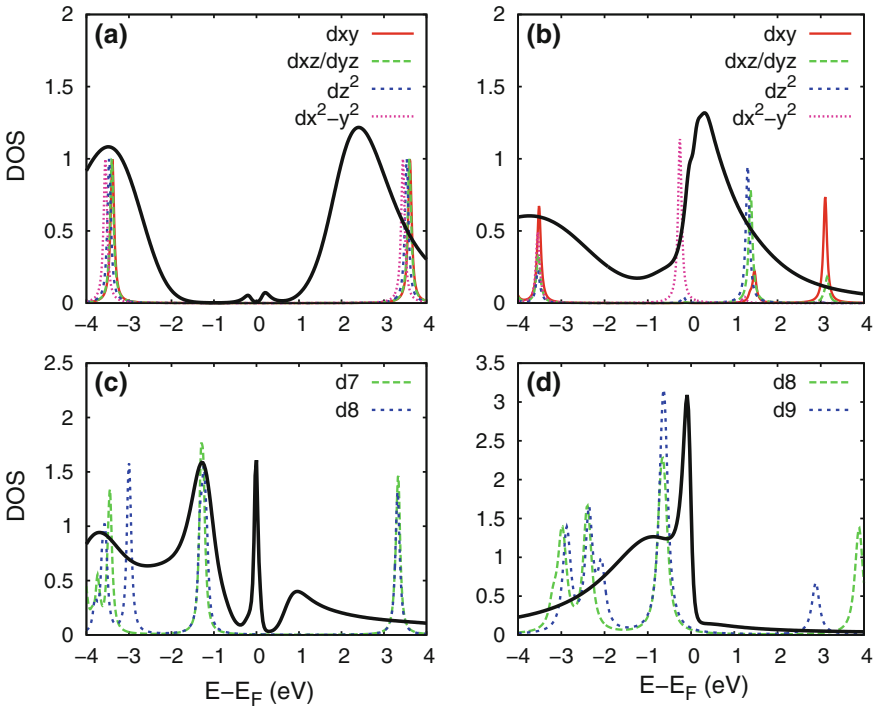

Fig. 3.7 DOS for Mn **a**, Fe **b**, Co **c** and Ni **d** impurities from QMC calculations (thick black lines) and from exact diagonalization (dashed lines) for different occupations of the d shell

multiplet $d^6 \rightarrow d^5$ excitations. The energy difference between photoemission peaks 1 and 2 can be understood from the ED results as splitting of the final d^5 multiplets: low-energy peak 2 is related to the $S = 5/2$, $L = 0$ state and high-energy peak 1 with the $S = 3/2$, $L \geq 0$ states. Moreover, we can estimate this energy difference as Jm, which relates to Hund's rule exchange.

Our theoretical QMC calculations for the Co adatom on Ag(100) with occupation $n = 7.8$ describe well the three-peak structure of the experimental photoemission spectrum (Fig. 3.6). The orbital character of the DOS from ED calculations (Fig. 3.7c) shows that the experimental peak 2 at -1 eV comes from excitations within the d_{xz}, d_{yz} and $d_{x^2-y^2}$ orbitals. Moreover, the high-energy experimental peak 1 is related to multi-orbital transitions between $d^8 \rightarrow d^7$ multiplets. Similar to the Fe case, the energy difference between peaks 1 and 2 is related to Hund's rule exchange and becomes smaller by J due to the different magnetic moment of Co.

The experimental and theoretical photoemission spectrum of the Ni adatom with only one broad peak below E_F is very different from other $3d$ impurities (Fig. 3.6). We can understand such a featureless spectrum from the Hund's rule physics related to a strong reduction of exchange splitting in Ni and very small splitting between atomic multiplets (Fig. 3.7d) which are washed out by hybridization with the substrate.

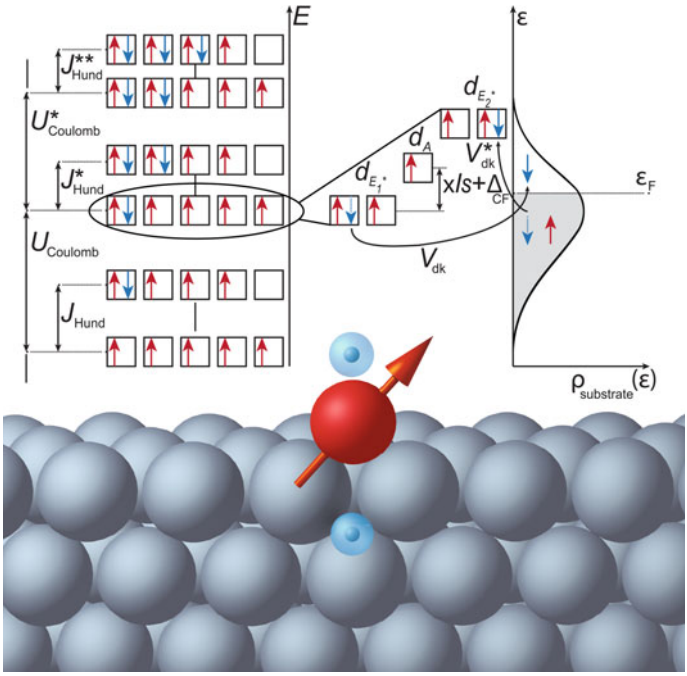

Fig. 3.8 Schematic view of a magnetic transition metal adatom (red) with additional hydrogens on a substrate. Top-left panel: The electronic spectrum with spin-up (red arrows) and spin-down (blue arrows) states of the five adatom 3*d* orbitals is filled up. The Hubbard energy U has to be paid if an additional electron is put into an orbital where there is already one, and Hund's rule energy J is paid if electron spins are flipped. Top-middle panel: Optimal electronic structure for the five orbitals in valance configurations with crystal field splitting Δ_{CF} and spin-orbit coupling ξls. Top-right panel: Hybridization parameter V_{dk} of the adatom orbitals with the substrate DOS $\rho_{substrate}$ which results in the broadening of impurity states

To understand why the experimental peak 2 for Fe, the peak 3 for Co and the broad peak for Ni are quite close to E_F, we investigate effects of valence fluctuations and formation of the Kondo resonance in 3*d* adatoms. One can see from Fig. 3.7b that for the d_{z^2} state of Fe there is only one peak in the DOS, just above the Fermi energy, without any signature of Hubbard bands. Moreover, the occupation of the Fe 3*d* shell of about $n = 6.4$ indicate strong charge fluctuations with mixed valence behavior. The similar situation applies for the Ni impurity where QMC calculations show broad spectra with strong renormalization of the quasiparticle peak towards E_F. Opposite to Fe and Ni, for the Co adatom on Ag(100) our results show much smaller charge fluctuations and the formation of Hubbard bands together with a sharp resonance at E_F which can be related to the multi-orbital Kondo effect. This conclusion is supported by STM spectroscopy of the Kondo resonance for a Co adatom on Ag(100) [21]. Similar correlation effects can be found for adatoms on insulating surfaces [23–28] and in f electron systems [29, 30].

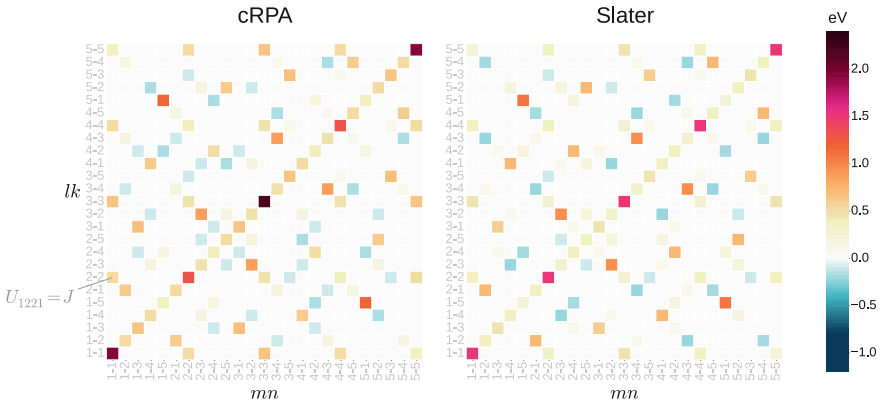

Fig. 3.9 Coulomb matrix for the d orbitals of the Co adatom obtained with the cRPA method (left) and subsequently rotationally averaged by the Slater approximation (right). The order of the orbitals is given by U_{mlkn}. The outlined element U_{1221} corresponds to the term $U_{1221} c^{+}_{1\uparrow} c^{+}_{2\downarrow} c_{2\downarrow} c_{1\uparrow}$, the index notation 1–5 refers to the orbital ordering $(d_{xy}, d_{yz}, d_{3z^2-r^2}, d_{xz}, d_{x^2-y^2})$

We can now discuss the concept of Hund's impurities [31] for the case of a $3d$ metal adatom on different substrates (Fig. 3.8). An isolated $3d$ atom corresponds to integer electronic configurations with occupation of different orbitals in accordance with the first Hund's rule. The different $3d$ states first are filled with spin-up electrons, and finally with spin-down electrons (Fig. 3.8). The reason for such configurations with maximal total spin is related with Hund's rule exchange energy J, which prevents a spin-flip process to a non-magnetic local configuration. For the case of a $3d$ transition metal adatom on a metallic substrate, electrons hybridize with the bath of conduction electrons with DOS $\rho_{\text{substrate}}$. This hybridization leads to fluctuations of the charge on the adatom. The strength of hybridization V_{dk} between the $3d$ adatom and itinerant k bands [32], and degree of valence fluctuations [22], will define whether the electronic state of the adatom can be described by atomic multiplets, itinerant bands, or both with specific correlation effects. In the case of weak hybridization $V_{\text{dk}} \approx 0$, the adatom electronic structure can be analyzed in terms of atomic multiplets with crystal field splittings Δ_{CF} and spin-orbit coupling ξls with integer valence occupations. For small hybridization the adatom still has the integer valency, but the Coulomb correlations lead to the formation of a Kondo singlet.

For large hybridization and the case of a single magnetic orbital, the adatom spin moment would be simply quenched by the conduction electrons. Nevertheless, for the case of multi-orbital $3d$ adatoms with relatively strong hybridization but smaller effects of J, profound charge fluctuations can coexist with large local magnetic moments, which are strongly coupled to the substrate. This situation may be referred to the Hund's impurity regime [4, 31]. It is characterized by a complex interplay of charge fluctuations, crystal field splitting, spin-orbit coupling, and electron correlations. The investigation of this regime was a challenge for the newly developed theoretical methods which we have explained [6]. Moreover, the experimental

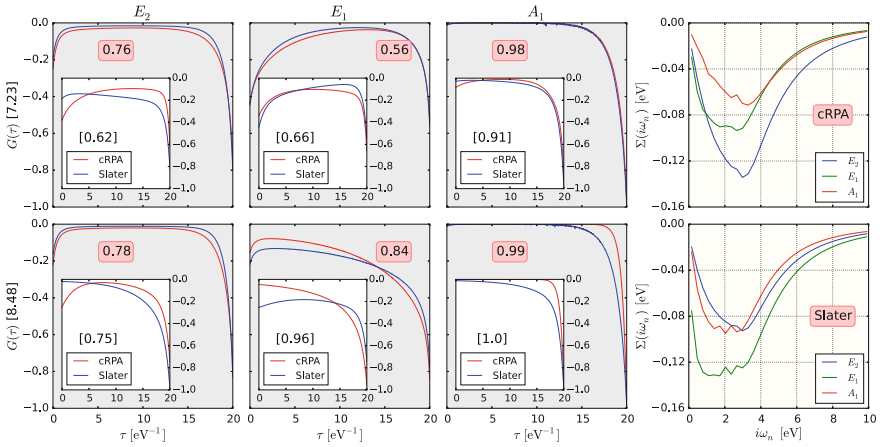

Fig. 3.10 Comparison between the representation-resolved imaginary-time Green's functions $G(\tau)$ for five d orbitals of the Co impurity calculated with the cRPA and the Slater Coulomb matrix. Total impurity occupations are given in squared brackets, orbital ones in round boxes. The upper row contains the full QMC Green's functions at lower filling together with the atomic solution in the insets (orbital occupations in brackets), and the lower row contains the corresponding Green's functions at higher filling. The filling can be adjusted by the double-counting chemical potential. The calculations were performed at $\beta = 20\,\mathrm{eV}^{-1}$, with the Matsubara self-energy $\Sigma(i\omega_n)$ (last column) for the different symmetry representations calculated with the cRPA (upper) and the Slater Coulomb matrix (lower), both at higher co filling

realization of a Hund's impurity, and, more importantly, the full control over all the relevant parameters, i.e. magnetic anisotropy, hybridization, temperature and magnetic field, had remained incomplete so far.

An important theoretical problem for correlated adatoms on substrates is related to the realistic representation for the Coulomb interaction vertex. The effective Coulomb interaction matrix screened by conduction electrons can be calculated using the so-called cRPA method [33]. All 625 elements of the cRPA Coulomb matrix U_{mlkn} constructed in this way are shown in Fig. 3.9 for the case of the $3d$ orbitals of cobalt adatoms on the graphene surface. If we compare the full U-matrix with the atomic-like Slater parametrisation based on the $U - J$ average interactions, one can clearly see the lower symmetry of the Coulomb vertex obtained from cRPA calculations.

Moreover, we can still find the numerically exact solution of the multi-orbital quantum impurity problem with anisotropic hybridization functions and the full Coulomb U-matrix using the CT-QMC scheme [6]. The imaginary-time of multi-orbital Green's functions obtained by the CT-QMC impurity solver are shown in Fig. 3.10. Let us compare results obtained with the cRPA and the Slater Coulomb matrix. Rotationally averaging the Coulomb matrix by the Slater approximation slightly reduces and redistributes the overall weight of the interaction strength (Fig. 3.9). The most pronounced differences occur for the higher filling considered, $n_{\mathrm{tot}} = 8.48$, especially in the A_1 representation. The hybridization in A_1 is small, thus the effect

entirely comes from the Coulomb interaction and its reduction in the spherical case. Lowering the Co filling by adjusting the chemical potential shows that the orbitals of E_1 symmetry change their occupation, and its main weight crosses the Fermi level. This is a consequence of the orbitals within this representation being the most hybridized as well as having the strongest partial screening of the Coulomb interaction. The self-energies show a characteristic Hund's impurity low-frequency metallic behaviour. As Co on graphene at higher Co filling of 8.48 is a Fermi-liquid, the self-energies should tend to zero at very low energies. This property is better resolved with the calculations using the cRPA matrix (Fig. 3.10). There is also a change of the order of the self-energy strengths between the orbitals of E_1 and E_2 symmetry, and they intersect in the cRPA case.

Finally, we mention that non-local generalizations of effective impurity models in the path-integral formalism [34–41] open up new directions for investigations of magnetic correlations and Kondo fluctuations [42–44]. The effects of long-range interactions are very important in graphene-based systems [45–53] and can be compared with different experimental data [54–58].

Acknowledgements We would like to thank Alexey Rubtsov, Mikhail Katsnelson, Tim Wehling, Frank Lechermann, Vladimir Mazurenko, Livio Chioncel, Hartmut Hafermann, Sergey Iskakov, Evgeny Gorelov, Alexander Rudenko, Yaroslav Kvashnin, Alexander Shick, Jindřich Kolorenč, Philipp Werner and Olle Eriksson for the intense and fruitful cooperation over the years. Financial support of this work by the Deutsche Forschungsgemeinschaft through the Sonderforschungsbereich 668 (project A3) is gratefully acknowledged.

References

1. N.W. Ashcroft, N.D. Mermin *Solid-State Physics* (Holt, Rinehart and Winston, University of California 1976), pp. 1–826
2. V.I. Anisimov, F. Aryasetiawan, A.I. Lichtenstein, J. Phys. Condens. Matter **9**, 767 (1997)
3. A. Damascelli, Z. Hussain, Z.-X. Shen, Rev. Mod. Phys. **75**, 473 (2003)
4. L. de Medici, J. Mravlje, A. Georges, Phys. Rev. Lett. **107**, 256401 (2011)
5. G. Kotliar, S.Y. Savrasov, K. Haule, V.S. Oudovenko, O. Parcollet, C.A. Marianetti, Rev. Mod. Phys. **78**, 865 (2006)
6. E. Gull, A.J. Millis, A.I. Lichtenstein, A.N. Rubtsov, M. Troyer, P. Werner, Rev. Mod. Phys. **83**, 349 (2011)
7. A. Hausoel, M. Karolak, E. Şaşıoğlu, A. Lichtenstein, K. Held, A. Katanin, A. Toschi, G. Sangiovanni, Nat. Commun. **8**, 16062 (2017)
8. R. Cardias, A. Szilva, A. Bergman, I. Di Marco, M.I. Katsnelson, A.I. Lichtenstein, L. Nordström, A.B. Klautau, O. Eriksson, Y.O. Kvashnin, Sci. Rep. **7**, 4058 (2017)
9. M.I. Katsnelson, VYu. Irkhin, L. Chioncel, A.I. Lichtenstein, R.A. de Groot, Rev. Mod. Phys. **80**, 315 (2008)
10. L. Chioncel, E. Arrigoni, M.I. Katsnelson, A.I. Lichtenstein, Phys. Rev. B **79**, 235123 (2009)
11. L. Chioncel, Y. Sakuraba, E. Arrigoni, M.I. Katsnelson, M. Oogane, Y. Ando, T. Miyazaki, E. Burzo, A.I. Lichtenstein, Phys. Rev. Lett. **100**, 086402 (2008)
12. A. Melnikov, I. Razdolski, T.O. Wehling, E.T. Papaioannou, V. Roddatis, P. Fumagalli, O. Aktsipetrov, A.I. Lichtenstein, U. Bovensiepen, Phys. Rev. Lett. **107**, 076601 (2011)
13. E.Y. Vedmedenko, N. Mikuszeit, T. Stapelfeldt, R. Wieser, M. Potthoff, A. Lichtenstein, R. Wiesendanger, Eur. Phys. J. B **80**, 331 (2011)

14. P.E. Blöchl, Phys. Rev. B **50**, 17953 (1994)
15. F. Lechermann, A. Georges, A. Poteryaev, S. Biermann, M. Posternak, A. Yamasaki, O.K. Andersen, Phys. Rev. B **74**, 125120 (2005)
16. B. Amadon, F. Lechermann, A. Georges, F. Jollet, T.O. Wehling, A.I. Lichtenstein, Phys. Rev. B **77**, 205112 (2008)
17. M. Karolak, T.O. Wehling, F. Lechermann, A.I. Lichtenstein, J. Phys. Condens. Matter **23**, 085601 (2011)
18. E. Gorelov, T.O. Wehling, A.N. Rubtsov, M.I. Katsnelson, A.I. Lichtenstein, Phys. Rev. B **80**, 155132 (2009)
19. B. Surer, M. Troyer, Ph. Werner, A.M. Läuchli, T.O. Wehling, A. Wilhelm, A.I. Lichtenstein, Phys. Rev. B **85**, 085114 (2012)
20. A.C. Hewson, J. Phys. Soc. Jpn. **74**, 8 (2005)
21. N. Knorr, M.A. Schneider, L. Diekhöner, P. Wahl, K. Kern, Phys. Rev. Lett. **88**, 096804 (2002)
22. S. Gardonio, M. Karolak, T.O. Wehling, L. Petaccia, S. Lizzit, A. Goldoni, A.I. Lichtenstein, C. Carbone, Phys. Rev. Lett. **110**, 186404 (2013)
23. V.V. Mazurenko, S.N. Iskakov, A.N. Rudenko, I.V. Kashin, O.M. Sotnikov, M.V. Valentyuk, A.I. Lichtenstein, Phys. Rev. B **88**, 085112 (2013)
24. A.N. Rudenko, V.V. Mazurenko, V.I. Anisimov, A.I. Lichtenstein, Phys. Rev. B **79**, 144418 (2009)
25. A.B. Shick, F. Máca, A.I. Lichtenstein, Phys. Rev. B **79**, 172409 (2009)
26. J. Honolka, A.A. Khajetoorians, V. Sessi, T.O. Wehling, S. Stepanow, J.-L. Mi, B.B. Iversen, T. Schlenk, J. Wiebe, N. Brookes, A.I. Lichtenstein, Ph. Hofmann, K. Kern, R. Wiesendanger, Phys. Rev. Lett. **108**, 256811 (2012)
27. M. Izquierdo, M. Karolak, C. Trabant, K. Holldack, A. Föhlisch, K. Kummer, D. Prabhakaran, A.T. Boothroyd, M. Spiwek, A. Belozerov, A. Poteryaev, A. Lichtenstein, S.L. Molodtsov, Phys. Rev. B **90**, 235128 (2014)
28. M. Karolak, M. Izquierdo, S.L. Molodtsov, A.I. Lichtenstein, Phys. Rev. Lett. **115**, 046401 (2015)
29. S. Gardonio, T.O. Wehling, L. Petaccia, S. Lizzit, P. Vilmercati, A. Goldoni, M. Karolak, A.I. Lichtenstein, C. Carbone, Phys. Rev. Lett. **107**, 026801 (2011)
30. E. Gorelov, J. Kolorenč, T. Wehling, H. Hafermann, A.B. Shick, A.N. Rubtsov, A. Landa, A.K. McMahan, V.I. Anisimov, M.I. Katsnelson, A.I. Lichtenstein, Phys. Rev. B **82**, 085117 (2010)
31. A.A. Khajetoorians, M. Valentyuk, M. Steinbrecher, T. Schlenk, A. Shick, J. Kolorenč, A.I. Lichtenstein, T.O. Wehling, R. Wiesendanger, J. Wiebe, Nat. Nanotech. **10**, 958 (2015)
32. C. Carbone, M. Veronese, P. Moras, S. Gardonio, C. Grazioli, P.H. Zhou, O. Rader, A. Varykhalov, P. Gambardella, S. Lebegue, O. Eriksson, M.I. Katsnelson, A.I. Lichtenstein, Phys. Rev. Lett. **104**, 117601 (2010)
33. F. Aryasetiawan, M. Imada, A. Georges, G. Kotliar, S. Biermann, A.I. Lichtenstein, Phys. Rev. B **70**, 195104 (2004)
34. A.N. Rubtsov, M.I. Katsnelson, A.I. Lichtenstein, Phys. Rev. B **77**, 033101 (2008)
35. S. Brener, H. Hafermann, A.N. Rubtsov, M.I. Katsnelson, A.I. Lichtenstein, Phys. Rev. B **77**, 195105 (2008)
36. H. Hafermann, M.I. Katsnelson, A.I. Lichtenstein, Europhys. Lett. **85**, 37006 (2009)
37. H. Hafermann, S. Brener, A.N. Rubtsov, M.I. Katsnelson, A.I. Lichtenstein, JETP Lett. **86**, 677 (2007)
38. M. Harland, M.I. Katsnelson, A.I. Lichtenstein, Phys. Rev. B **94**, 125133 (2016)
39. A.N. Rubtsov, M.I. Katsnelson, A.I. Lichtenstein, Ann. Phys. **327**, 1320 (2012)
40. H. Hafermann, G. Li, A.N. Rubtsov, M.I. Katsnelson, A.I. Lichtenstein, H. Monien, Phys. Rev. Lett. **102**, 206401 (2009)
41. H. Hafermann, Ch. Jung, S. Brener, M.I. Katsnelson, A.N. Rubtsov, A.I. Lichtenstein, Europhys. Lett. **85**, 27007 (2009)
42. N. Néel, J. Kröger, R. Berndt, T. Wehling, A. Lichtenstein, M.I. Katsnelson, Phys. Rev. Lett. **101**, 266803 (2008)

43. N. Néel, R. Berndt, J. Kröger, T.O. Wehling, A.I. Lichtenstein, M.I. Katsnelson, Phys. Rev. Lett. **107**, 106804 (2011)
44. M. Karolak, D. Jacob, A.I. Lichtenstein, Phys. Rev. Lett. **107**, 146604 (2011)
45. T.O. Wehling, S. Yuan, A.I. Lichtenstein, A.K. Geim, M.I. Katsnelson, Phys. Rev. Lett. **105**, 056802 (2010)
46. T.O. Wehling, E. Şaşıoğlu, C. Friedrich, A.I. Lichtenstein, M.I. Katsnelson, S. Blügel, Phys. Rev. Lett. **106**, 236805 (2011)
47. T.O. Wehling, A.I. Lichtenstein, M.I. Katsnelson, Phys. Rev. B **84**, 235110 (2011)
48. B. Sachs, T.O. Wehling, M.I. Katsnelson, A.I. Lichtenstein, Phys. Rev. B **84**, 195414 (2011)
49. T.O. Wehling, M.I. Katsnelson, A.I. Lichtenstein, Chem. Phys. Lett. **476**, 125 (2009)
50. T.O. Wehling, I. Grigorenko, A.I. Lichtenstein, A.V. Balatsky, Phys. Rev. Lett. **101**, 216803 (2008)
51. T.O. Wehling, A.V. Balatsky, A.M. Tsvelik, M.I. Katsnelson, A.I. Lichtenstein, Europhys. Lett. **84**, 17003 (2008)
52. T.O. Wehling, A.V. Balatsky, M.I. Katsnelson, A.I. Lichtenstein, K. Scharnberg, R. Wiesendanger, Phys. Rev. B **75**, 125425 (2007)
53. T.O. Wehling, A.I. Lichtenstein, M.I. Katsnelson, Appl. Phys. Lett. **93**, 202110 (2008)
54. T.O. Wehling, K.S. Novoselov, S.V. Morozov, E.E. Vdovin, M.I. Katsnelson, A.K. Geim, A.I. Lichtenstein, Nano Lett. **8**, 173 (2008)
55. S.J. Altenburg, J. Kröger, T.O. Wehling, B. Sachs, A.I. Lichtenstein, R. Berndt. Phys. Rev. Lett. **108**, 206805 (2012)
56. L.V. Dzemiantsova, M. Karolak, F. Lofink, A. Kubetzka, B. Sachs, K. von Bergmann, S. Hankemeier, T.O. Wehling, R. Frömter, H.P. Oepen, A.I. Lichtenstein, R. Wiesendanger, Phys. Rev. B **84**, 205431 (2011)
57. M. Gyamfi, T. Eelbo, M. Waśniowska, T.O. Wehling, S. Forti, U. Starke, A.I. Lichtenstein, M.I. Katsnelson, R. Wiesendanger, Phys. Rev. B **85**, 161406 (2012)
58. T. Eelbo, M. Waśniowska, P. Thakur, M. Gyamfi, B. Sachs, T.O. Wehling, S. Forti, U. Starke, C. Tieg, A.I. Lichtenstein, R. Wiesendanger, Phys. Rev. Lett. **110**, 136804 (2013)